

Cite this article as: Li Qindong, Meng Junsheng, Chen Baisen, et al. Cyclic-Oxidation Behavior of CeO₂-Modified Aluminide Coating on 309 Stainless Steel[J]. Rare Metal Materials and Engineering, 2023, 52(11): 3707-3714. DOI: 10.12442/j.issn.1002-185X.20230205.

ARTICLE

Cyclic-Oxidation Behavior of CeO₂-Modified Aluminide Coating on 309 Stainless Steel

Li Qindong, Meng Junsheng, Chen Baisen, Hao Chenfan, Chen Zhihui

Naval Architecture & Port Engineering College, Shandong Jiaotong University, Weihai 264200, China

Abstract: A CeO₂-modified aluminide coating was prepared on 309 stainless steel by pack cementation method with NH₄Cl as activator. The surface and cross-section of the coating before and after cyclic-oxidation at 900 °C for 50 cycles were analyzed by X-ray diffractometer and scanning electron microscope coupled with energy dispersive spectroscopy. The microstructure analysis results show that the modified coating consists of Fe₄Al₁₃ phase. A few CeO₂ nanoparticles are entrapped due to the outward diffusion of base metal. Compared with the normal aluminide coating without the addition of CeO₂ nanoparticles, the aluminide coating modified by dispersed CeO₂ nanoparticles has better scale spallation resistance in air at 900 °C. Some Fe₂Al₅ phases can be found on CeO₂-modified aluminide coating even after 50 cycles of oxidation. Additionally, the outward-diffused Al layer, the intermediate FeAl layer, and the external Fe₂Al₅+FeAl mixed layer exist in the coating, suggesting that CeO₂ nanoparticles can retard the degradation of aluminide coatings.

Key words: pack cementation; aluminide coating; reactive element effect; cyclic-oxidation

309 stainless steel with higher Cr content (23.2wt%) and Ni content (13.1wt%) is widely used in boiler and chemical industries at temperatures below 980 °C due to its excellent mechanical properties and perfect corrosion resistance, which is caused by the thermal growth of protective chromic scale^[1-2]. The volatile CrO₃ usually forms at temperature above 900 °C^[3]. In this case, the integrity of protective chromic scale is destroyed and a non-protective Fe-rich oxide scale forms. Normally, the aluminide coatings are used for the FeAl composite to enhance its oxidation resistance at above 1000 °C^[4-6]. However, the aluminizing at high temperatures inevitably degrades the mechanical properties of workpieces. Therefore, the low temperature aluminide coatings are proposed^[7-12], which usually consist of Fe₂Al₅ or FeAl₃ phases and exhibit good oxidation resistance^[9-11]. The scale properties can be further enhanced^[13-15] through the trace addition of rare earth oxides, such as Y₂O₃, CeO₂, and La₂O₃, by different methods before aluminizing. The methods include ion implantation^[16], sol-gel^[17], and co-deposition of rare earth oxides with Ni^[10,13-14]. However, these methods cannot be used for practical

manufacture. Recently, with the rare earth oxides as fillers, the reactive-element-modified aluminide coatings attract much attention, such as TC4 coating at 1000 °C^[18-19], Ni coating at 800 °C^[20-21], GH586 coating at 800 °C^[22], IN-738 LC coating at 760 °C^[23-24], carbon steel coating at 650 °C^[25], and Ni-18Fe-17Cr and Fe-18Cr-9Ni alloy coatings at 520–600 °C through ball peening^[26]. According to Ref.[27–28], the entrapped Y₂O₃ at 600–700 °C not only decreases the scaling rate, but also enhances the scale adhesion of aluminide coatings.

In this research, a CeO₂-dispersed aluminide coating was prepared on 309 stainless steel at 800 °C for 4 h and the effects of CeO₂ addition on coating formation and cyclic-oxidation resistance were investigated.

1 Experiment

The specimens with size of 20 mm×10 mm×2 mm were cut from the commercial 309 stainless steel with nominal composition of 0.08C-1.00Si-2.00Mn-23.20Cr-13.10Ni-0.045P-0.030S-Fe (wt%). The specimens were ground by 800# SiC paper, ultrasonically cleaned by acetone, and

Received date: April 12, 2023

Foundation item: Natural Science Foundation of Shandong Province (ZR2019MEE107); Project of Shandong Provincial Department of Transportation (2020B88); Graduate Science and Technology Innovation Project of Shandong Jiaotong University (2023YK106, 2023YK109)

Corresponding author: Meng Junsheng, Ph. D., Associate Professor, Naval Architecture & Port Engineering College, Shandong Jiaotong University, Weihai 264200, P. R. China, Tel: 0086-631-3998910, E-mail: 222011@sdjtu.edu.cn

Copyright © 2023, Northwest Institute for Nonferrous Metal Research. Published by Science Press. All rights reserved.

aluminized in the mixtures of 50wt% Al+45wt% inert filler (45wt% Al_2O_3 or 35wt% Al_2O_3 +10wt% CeO_2)+5wt% NH_4Cl under Ar gas at 800 °C for 4 h. The powders of Al, Al_2O_3 , and NH_4Cl were commercial powders with purity of 99.8%, and the CeO_2 particles were pure nanoparticles (purity of 99.9%) with average size of 40 nm. Transmission electron microscope (TEM) and selected area electron diffractometer (SAED) were used to observe the microstructures of CeO_2 nanoparticles. Fig.1 shows TEM morphologies and SAED pattern of CeO_2 nanoparticles. After aluminizing, all specimens were ultrasonically cleaned by acetone and then washed by distilled water. The base metal and the coatings without and with CeO_2 nanoparticles are denoted as SS, AS, and CAS, respectively.

Cyclic-oxidation test was conducted at 900 °C in air in a vertical furnace with an automatic specimen-lifting system. The specimens were lifted from the furnace every 60 min high-temperature oxidation exposure and then cooled in air for 15 min, and this process was denoted as one oxidation cycle. After certain cycles, the oxidized specimens were weighed by a balance (accuracy: 0.01 mg). The mass gain was represented by the average value of three parallel specimens. The phases and composition of different specimens before and after cyclic-oxidation were analyzed by X-ray diffractometer (XRD, D/Max-2500 pc) and scanning electron microscope (SEM) coupled with X-ray energy dispersive spectroscopy (EDS, Camscan MX2600FE).

2 Results and Discussion

2.1 Microstructure of aluminide coating

Fig. 2 shows SEM morphologies and corresponding EDS results of AS and CAS specimens. Clearly, AS specimen presents the nodular grain structures with mean size of 4.5 μm (Fig. 2a); whereas CAS specimen exhibits the fine spherical

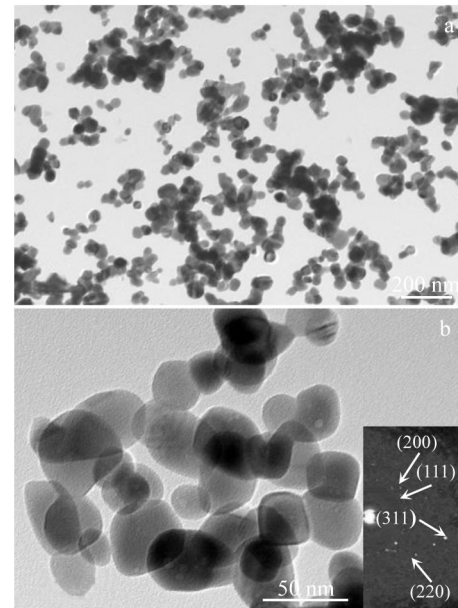


Fig.1 TEM morphologies and SAED pattern of CeO_2 nanoparticles

grain structures with uneven surface (Fig. 2c). According to EDS results of Fig. 2b and 2d, the average Al content for AS and CAS specimens is approximately 75at%, which corresponds to FeAl_3 phase. Fig. 3 shows XRD patterns of different specimens. It can be seen that the Al-rich Fe_4Al_3 phase exists in the coatings. The Ce in CAS specimen (Fig. 2d) indicates that some CeO_2 nanoparticles are successfully entrapped into the aluminide coatings.

Fig. 4 shows the cross-sectional morphologies of AS and CAS specimens. Clearly, specimen AS exhibits a flat surface and the coating thickness is approximately 200 μm (Fig. 4a). However, specimen CAS exhibits an uneven surface with a

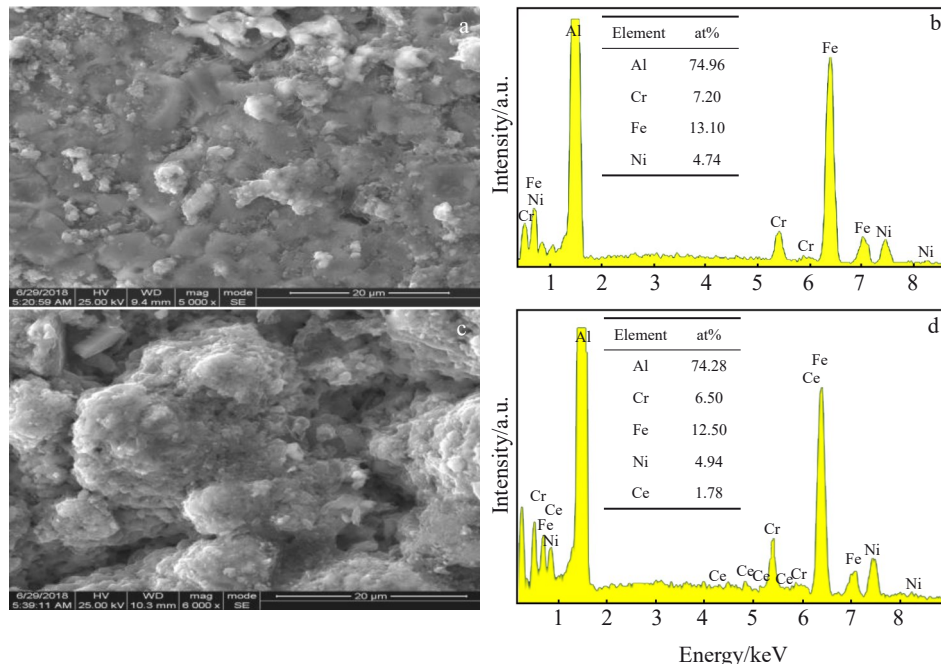


Fig.2 Surface morphologies (a, c) and corresponding EDS results (b, d) of AS specimen (a–b) and CAS specimen (c–d)

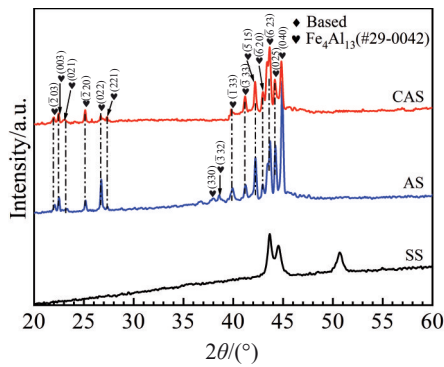


Fig.3 XRD patterns of SS, AS, and CAS specimens

thinner coating thickness of approximately 170 μm (Fig. 4c). Fig.4b and 4d show that both aluminide coatings have a two-layer structure: an outer layer with cracks formed during cross-sectional preparation process and an inner layer with dispersed bright phases. Compared with the inner layer, the outer layer has higher Al content and lower Fe and Cr contents, as shown in Fig. 5. Furthermore, the Cr content

fluctuates in the inner layer and it is increased with decreasing the Fe and Al contents at bright phases, suggesting that these bright phases are Cr-rich phases. EDS results further prove that the average composition of the outer layer and inner layer is 75Al-6.5Cr-13.5Fe-5Ni (at%) and 68Al-10Cr-15Fe-7Ni (at%), which is close to that of $\text{Fe}_3\text{Al}_{14}$ and Fe_2Al_5 phases^[29], respectively. However, only the characteristic peaks of $\text{Fe}_4\text{Al}_{13}$ phase can be detected in Fig.3. This is because the inner layer with bright Cr-rich phases is beyond the XRD detection depth. Therefore, no Fe_2Al_5 or other Cr-rich phases can be detected.

Fig. 6a shows the typical cross-sectional morphology of outer layer in CAS specimen after etching. Clearly, the white nanoparticles can be observed. According to Fig.6b, the white nanoparticles have higher Ce content compared with EDS results in Fig.2d, suggesting that these white particles are the entrapped CeO_2 nanoparticles.

2.2 Cyclic-oxidation

Fig. 7 shows the mass changes of different specimens at 900 °C during cyclic-oxidation in air. For SS specimen, a nearly liner mass loss occurs due to the severe scale spallation. The mass change reaches -7.59 mg/cm^2 after 50

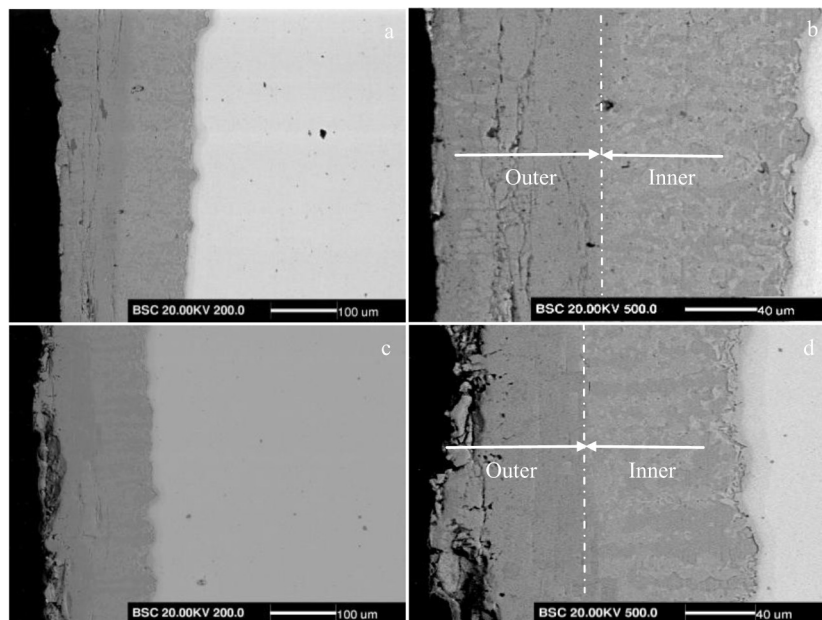


Fig.4 Cross-sectional morphologies of AS specimen (a–b) and CAS specimen (c–d)

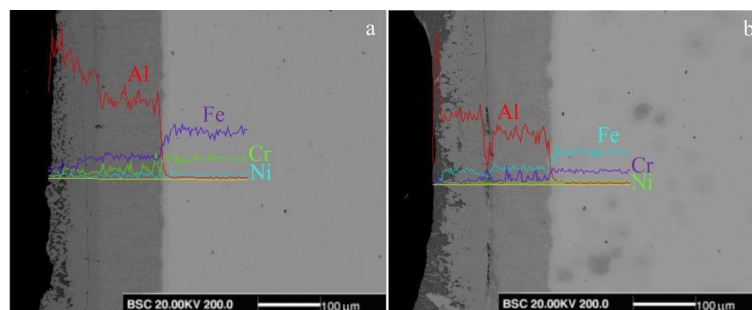


Fig.5 Cross-sectional morphologies and EDS line scanning results of AS specimen (a) and CAS specimen (b)

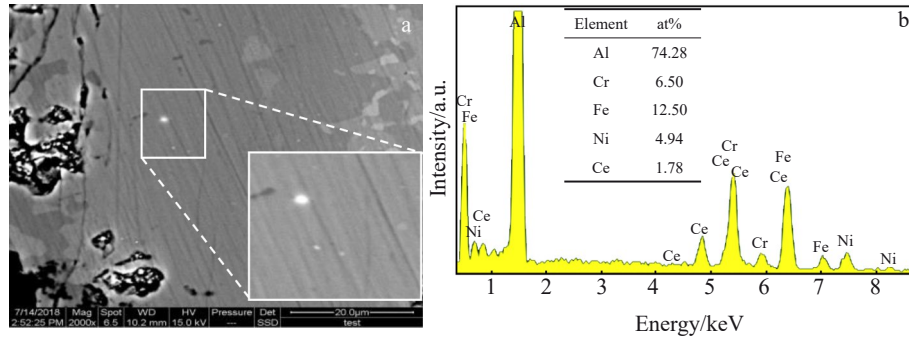


Fig.6 Cross-sectional morphology of outer layer in CAS specimen (a); EDS results of white particles in the rectangular area of Fig.6a (b)

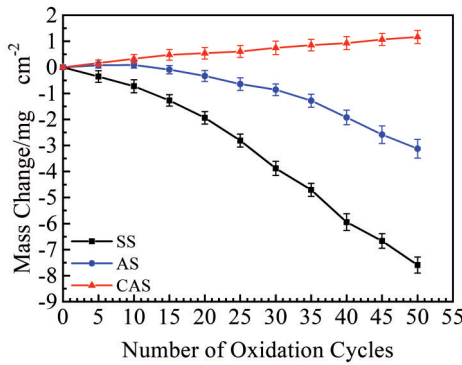


Fig.7 Mass changes of SS, AS, and CAS specimens during cyclic-oxidation at 900 °C for 50 cycles

cycles, indicating the worst scale adhesion. For AS specimen, the mass gain is 0.09 mg/cm² after 10 cycles, and then the mass loss occurs due to the initiation of scale spallation. After 50 cycles, its mass change reaches -3.12 mg/cm², indicating a better scale adhesion compared with that of SS specimen. However, for CAS specimen, a steady mass gain curve can be observed: no scale spallation occurs and the mass gain after 50 cycles is only 0.36 mg/cm², suggesting the optimal scale adhesion.

Fig. 8 shows XRD patterns of different specimens after cyclic-oxidation tests at 900 °C for 50 cycles. Clearly, in SS specimen, some mixture scales of FeCr₂O₄ with minor Fe₂O₃

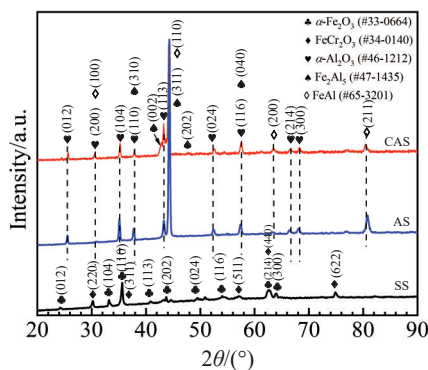


Fig.8 XRD patterns of oxide scales formed on SS, AS, and CAS specimens after cyclic-oxidation at 900 °C for 50 cycles

are formed. However, only Al₂O₃ can be detected in AS and CAS specimens. Furthermore, both AS and CAS aluminide coatings are completely degraded into FeAl without and with minor Fe₂Al₃, respectively. The existence of Fe₂Al₃ phases in CAS specimen suggests that the entrapped CeO₂ nanoparticles can significantly retard the degradation degree.

SEM surface morphologies of different oxidized specimens after cyclic-oxidation at 900 °C for 50 cycles are shown in Fig. 9. Clearly, heavy spallation occurs on SS specimen (Fig. 9a), indicating the worse scale adhesion. Fig. 9b shows the magnified image of the spallation area of Fig. 9a, where the coarse grain with higher Fe content can be observed, indicating the regeneration of non-protective Fe-rich scales at the spallation area. For AS specimen, the oxide scales in the central area of specimens are porous with minor spallation (Fig. 9c). The oxides are round Al-rich phases, according to EDS results. Based on XRD results in Fig. 8, the round oxides are α -Al₂O₃ phase. However, obvious spallation can be observed at the corners of AS specimen (Fig. 10a). At the spallation area, some whisker- and needle-like oxides can be observed (Fig. 10b). These oxides are θ -Al₂O₃ phase, according to Ref. [10–14], which cannot be detected by XRD due to its low content. For CAS specimen, only compact round α -Al₂O₃ phase without scale spallation and cracks can be observed (Fig. 9e–9f).

Fig. 11 shows the cross-sectional image of the oxide scales formed on SS specimen and EDS line scanning results. Clearly, a thicker scale of approximately 20 mm in thickness with significant cracks exists in SS specimen, and the delamination and spallation phenomena occur, suggesting the worst scale adhesion. Additionally, the outer scale is Fe-rich layer, and the inner scale is Cr-rich layer. Based on Fig. 8, the outer scale is Fe₂O₃ with solid solution of Cr and the inner scale is FeCr₂O₄, which are consistent with the results in Ref. [27].

For AS specimen, a thin alumina scale of 4.5 mm in thickness with some voids, cracks, and internal oxidation can be observed, as shown in Fig. 12, suggesting the improved scale adhesion. At the same time, the coating exhibits a two-layer structure: bright inner layer I and gray outer layer II. EDS spectra indicate that the gray outer layer has a high and stable Al content, whereas the Al content is sharply decreased in the bright inner layer. Based on XRD results in Fig. 8, the

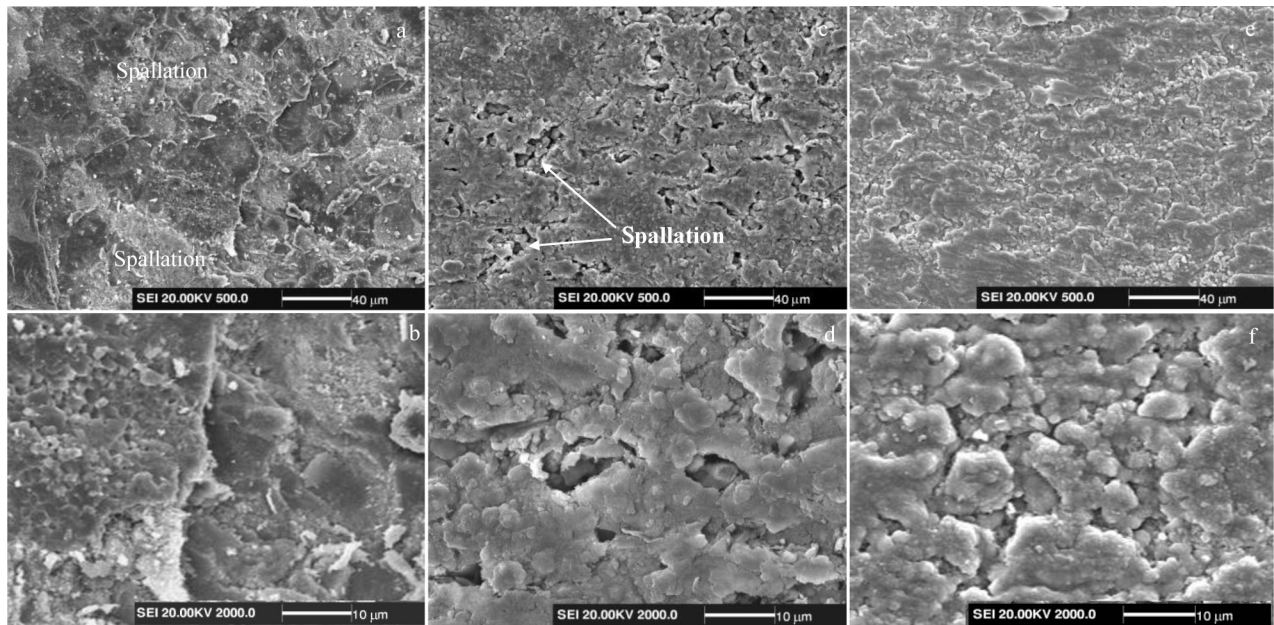


Fig.9 SEM surface morphologies of oxide scales formed on SS specimen (a–b), AS specimen (c–d), and CAS specimen (e–f) after cyclic-oxidation at 900 °C for 50 cycles

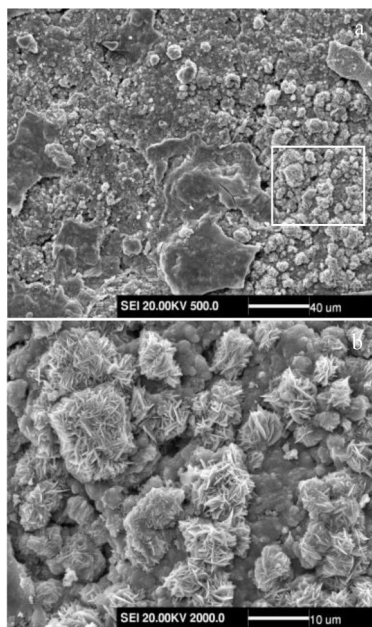


Fig.10 Surface morphology of oxide scales formed at the corner of AS specimen (a); magnified image of the rectangular area in Fig.10a (b)

outer layer is FeAl layer and the inner layer is inward-diffused Al layer. It is worth noting that the high Ni content and low Cr content appear at II/I interface, and the high Cr content appears in the layer I close to II/I interface. This result indicates that the inward diffusion of Al increases the Cr content near the interface.

Based on the abovementioned results, it can be deduced that AS specimen is completely degraded to FeAl phase after cyclic-oxidation for 50 cycles. In contrast, CAS specimen

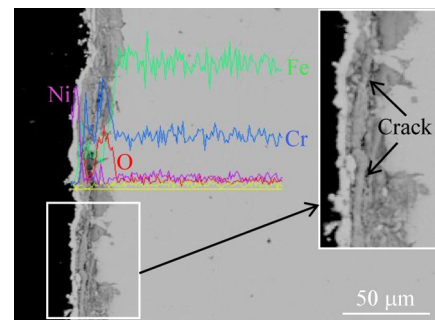


Fig.11 Cross-sectional morphologies and EDS line scanning results of oxide scales formed on SS specimen after cyclic-oxidation at 900 °C for 50 cycles

forms a thinner scale with minor internal oxidation, as shown in Fig.13a, indicating the optimal scale adhesion. At the same time, CAS is degraded into three layers: black-and-gray-mixed outer layer III, gray middle layer II, and bright inner layer I. After etching, some white particles appear at the black/gray phase interface (Fig.13b). EDS line scanning results indicate that these white nanoparticles are Ce-rich dispersed nanoparticles, which may be the original CeO₂ nanoparticles or the precipitated CeO₂ nanoparticles due to the lower solubility of CeO₂ in FeAl phase. According to Fig.13c, the black phases have higher Al content (70.5at%) than the gray phases (49.5at%) do, which correspond to Fe₂Al₃ and FeAl phases, respectively. Therefore, the black-and-gray-mixed outer layer III is the FeAl+Fe₂Al₃ mixed layer. The gray middle layer II is FeAl layer and the bright inner layer I is the inward-diffused Al layer with a sharply decreasing Al content. As shown in Fig.13a and 13c, it can be found that the black Fe₂Al₃ phases nearly form a continuous layer beneath the oxide scale of 29

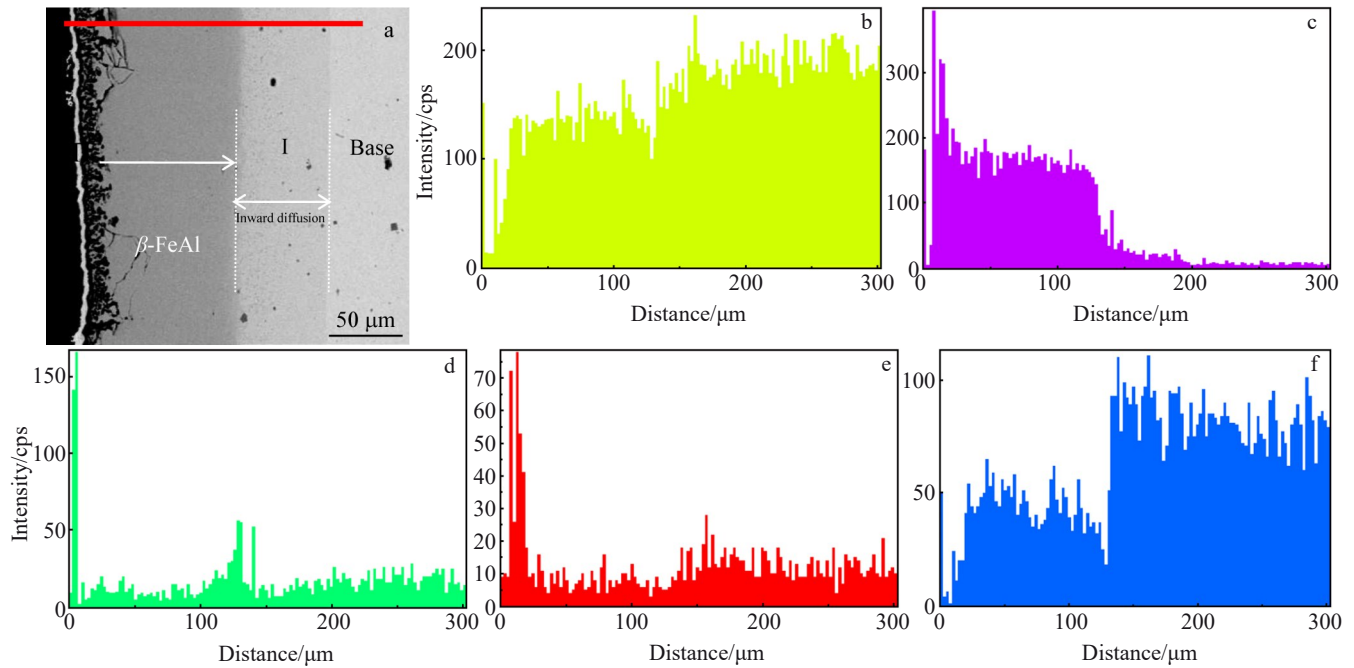


Fig.12 SEM cross-sectional microstructure of oxide scales formed on AS specimen after cyclic-oxidation at 900 °C for 50 h (a); EDS line scanning results of Fe (b), Al (c), Ni (d), O (e), and Cr (f) elements along the line marked in Fig.12a

mm in depth and at III/II interface. The distance from the black Fe_2Al_5 layer to III/II interface is approximately 74 μ m.

2.3 Discussion

Fig.3 indicates that both AS and CAS specimens have the similar single $\text{Fe}_4\text{Al}_{13}$ phase. Fig.4 indicates that the aluminide coatings have the two-layer structures^[27-28]. The outer layer is $\text{Fe}_4\text{Al}_{13}$ phase with minor Cr and Ni and its formation is attributed to the outward diffusion of base metal. The inner layer is the inward-diffused Al layer with bright Cr-rich dispersed particles^[27-28]. The outward growth of outer layer entraps some CeO_2 nanoparticles into the aluminide layer (Fig. 6 and Fig. 2c), and they are dispersed along the grain boundaries of aluminide, consequently hindering the grain growth of aluminide (Fig. 2c). Furthermore, the entrapped CeO_2 nanoparticles show the inhibition effect^[23-24,28] to reduce the aluminide coating thickness and even to form an uneven^[28]

or discontinuous coating^[23].

For SS specimen, the Cr-rich scale forms immediately once the oxidation starts due to the higher Cr content (23.2wt%). However, the reaction of Cr_2O_3 with O_2 above 900 °C causes the formation of volatile CrO_3 , which destroys the protective of chromic scale^[3]. When the Cr content below the scale is lower than the critical content required for the growth of chromic layer, non-protective Fe-rich scale with high scaling rate can be formed (Fig. 8 and Fig. 11). The higher thermal stress during cooling causes the cracking and spallation phenomena of Fe-rich oxide scales because of their lower ductility^[30]. This is why the scale spallation even occurs only after 5 cycles of high-temperature oxidation (Fig.7). The scale spallation exposes the underlying coating to the air. The regeneration of Fe-rich oxide scale and its spallation during cyclic-oxidation cause the further mass loss. Consequently, a steady mass loss can be observed after cyclic-oxidation for 5

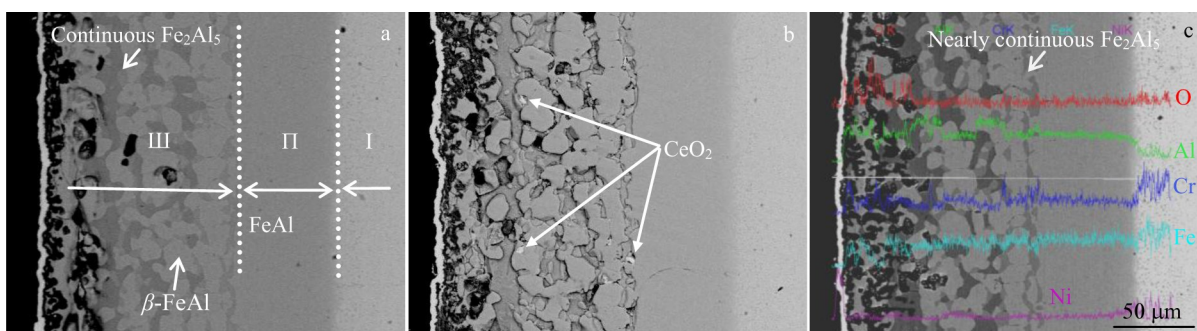


Fig.13 Cross-sectional morphologies of oxide scales formed on CAS specimen after cyclic-oxidation at 900 °C for 50 cycles before (a) and after (b) etching; EDS line scanning results of oxide scales formed on CAS specimen after cyclic-oxidation at 900 °C for 50 cycles after etching (c)

cycles. Briefly, SS specimen exhibits poor scale adhesion and the worst scale spallation resistance in this research.

Generally, the alumina scale adhesion is inherently correlated with the formation of large interface cavities at the scale/metal interface^[31]. The formation of large interface cavities greatly decreases the critical stress for scale decohesion^[32]. The high thermal stress during cyclic-oxidation causes the cracking and spallation of scales. For AS specimens, the scale spallation occurs after 10 cycles of oxidation, mainly at the corners of AS specimens (Fig.10). At the spallation area, minor whisker-like θ -Al₂O₃ phase with high oxidation rate forms^[11,13-14]. After 10 cycles of oxidation, a steady minor mass loss occurs (Fig. 7) due to the scale spallation (Fig. 9c). A thicker alumina scale of 4.5 mm in thickness with voids, cracking, and spallation appears. Additionally, the internal oxidation occurs (Fig. 12), suggesting the enhanced scale adhesion, compared with that of SS specimen. However, no scale spallation occurs on CAS specimen during 50 cycles of oxidation and a thinner scale with less voids and minor internal oxidation forms, suggesting the optimal scale adhesion in this research. There are several reasons for the optimal scale adhesion, and they are discussed as follows.

Firstly, the entrapped CeO₂ nanoparticles can refine the aluminide grains (Fig. 2c)^[10,13-14,20-21,27-28], which significantly increases the sites for alumina nucleation and thereby causes the growth of fine-grained scale with improved plastic deformation capacity and lower thermal stresses^[33]. Furthermore, the grain refinement also decreases the interface voiding kinetics by providing more sites for the condensation of vacancies or by minimizing the flux of Kirkendal vacancies towards the interface^[33]. Thus, the aluminide coatings with fine grain structures will intrinsically form the adherent scale. Secondly, the inward growth of alumina scale can entrap some CeO₂ nanoparticles into the scale^[13-14,27-28], and they partially dissolve to produce Ce cations^[34]. The Ce cations dispersed along the grain boundaries can block the outward diffusion of Al element, thereby decreasing the oxidation rate and forming the adherent scale with less interface voids^[33]. Thirdly, Ce ions or CeO₂ nanoparticles dispersed along the grain boundary can refine the scale grains through solute-drag effect, thereby enhancing scale adhesion. Fourthly, the CeO₂ nanoparticles act as the sinks for vacancies^[13,35] to decrease the interface voiding kinetics, thereby increasing the scale adhesion. Last but not least, the CeO₂ nanoparticles decrease the segregation of sulfur at the scale/matrix interface, therefore improving the scale adhesion^[35].

The formation of alumina scale and the interdiffusion lead to the degradation of aluminide coatings. The initial thicker aluminide coating on AS specimen is transformed to the FeAl phase after 50 cycles of oxidation and the two-layer structure can be observed^[28]: the FeAl outer layer and the inward-diffused Al inner layer (Fig. 8 and Fig. 12). In contrast, some Fe₂Al₅ phases can still be found in CAS specimen even after 50 cycles of oxidation (Fig. 8 and Fig. 13) and a three-layer structure can be observed^[28]: the inward-diffused Al zone, the

middle FeAl layer, and the outer Fe₂Al₅+FeAl mixed layer, suggesting that CeO₂ nanoparticles reduce the degradation of coatings. This is because the addition of CeO₂ nanoparticles improves the scale adhesion, thereby decreasing the consumption of Al element by oxidation. Besides, the interdiffusion-induced interface movement^[28] causes the accumulation of CeO₂ nanoparticles at black Fe₂Al₅/gray FeAl interface (Fig. 13b), which can act as ceramics^[36] to hinder the degradation of Fe₂Al₅ phase into FeAl phase. This is why the nearly continuous thin Fe₂Al₅ layer can also be observed at III/II interface with dispersed CeO₂ nanoparticles.

3 Conclusions

1) Both normal aluminide coating and CeO₂-modified aluminide coating on 309 stainless steel have the similar two-layer structures: the outer Fe₄Al₁₃ layer with minor Cr and Ni elements and the inner layer with the dispersion of bright Cr-rich phases.

2) The CeO₂ nanoparticles entrapped into the outer layer cannot only refine the grains, but also exert the inhibition effect on the coating formation.

3) The fine-grain CeO₂-dispersed aluminide coatings can intrinsically form the adherent scale.

4) The entrapped CeO₂ nanoparticles can reduce the degradation of aluminide coatings.

References

- 1 Cui T M, Xu X H, Pan D et al. *Journal of Nuclear Materials*[J], 2022, 561: 153 509
- 2 Wei Shuchao, Li Mingyu, Zhan Zhaolin. *Rare Metal Materials and Engineering*[J], 2022, 51(12): 4697 (in Chinese)
- 3 Menzies I A, Mortimer D. *Corrosion Science*[J], 1966, 6(11-12): 517
- 4 Paul B, Jagannadh S V S N, Majumdar S et al. *Materials Today Proceedings*[J], 2016, 3(9): 3178
- 5 Huang J Y, Lu J T, Zhang X X et al. *Metallurgical and Materials Transactions A*[J], 2019, 50: 3776
- 6 Yang Z, Lu J T, Zhang P et al. *Surface and Coatings Technology*[J], 2020, 391: 125 700
- 7 Xiang Z D, Datta P K. *Acta Materialia*[J], 2006, 54: 4453
- 8 Zhan Z L, He Y D, Wang D R et al. *Intermetallics*[J], 2006, 739: 12 132
- 9 Bates B L, Wang Y Q, Zhang Y et al. *Surface and Coatings Technology*[J], 2009, 204(6-7): 766
- 10 Zhou Y B, Hu H T, Zhang H J et al. *Vacuum*[J], 2011, 86(2): 210
- 11 Zheng L, Peng X, Wang F. *Corrosion Science*[J], 2011, 53(2): 597
- 12 Kumar S, Majumdar S, Paul B et al. *Surface and Coatings Technology*[J], 2021, 426: 127 794
- 13 Xu C, Peng X, Wang F. *Corrosion Science*[J], 2010, 52(3): 740
- 14 Peng X, Guan Y, Dong Z et al. *Corrosion Science*[J], 2011, 53(5): 1954
- 15 Pfeil B. *UK Patent*, 459848[P], 1937
- 16 Simon C R, Seiersten M, Caron P et al. *Materials Science*

- Forum[J], 1997, 251–254: 429
- 17 Hampikian J M. *Oxidation of Metals*[J], 1998, 50: 123
- 18 Zhou W, Zhao Y G, Li W et al. *Materials Science and Engineering A*[J], 2007, 458(1–2): 34
- 19 Li X, Tian J, Tian W et al. *Oxidation of Metals*[J], 2018, 89: 471
- 20 Zhang H J, Sun J F. *Rare Metal Materials and Engineering*[J], 2015, 44(11): 2628
- 21 Zhang H J, Sun J F. *Rare Metal Materials and Engineering*[J], 2017, 46(2): 301
- 22 Hua Y Q, Rong Z, Chen K M et al. *Advanced Materials Research*[J], 2015, 1095: 603
- 23 Ebadi F, Nogorani F S, Fatemi F et al. *Metallurgical and Materials Transactions A*[J], 2020, 51: 5958
- 24 Fatemi F, Nogorani F S et al. *Corrosion Science*[J], 2022, 196: 110 031
- 25 Mobin M, Sharma H K, Hasan S K et al. *Anti-corrosion Methods and Materials*[J], 2002, 49(4): 283
- 26 Zhan Z L, He Y D, Gao W et al. *Acta Metallurgica Sinica (English Letters)*[J], 2006, 19(3): 215
- 27 Wang Y D, Wang J X, Hu H T et al. *Vacuum*[J], 2018, 155: 193
- 28 Wang Y D, Wang J X, Hu H T et al. *Vacuum*[J], 2018, 158: 101
- 29 Thiers L, Mukasyan A S, Varma A et al. *Combustion and Flame*[J], 2002, 131: 198
- 30 Zhou C H, Liu A L, Ma H T et al. *Oxidation of Metals*[J], 2016, 86: 537
- 31 Hou P Y, Priimak K. *Oxidation of Metals*[J], 2005, 63: 113
- 32 Hancock P, Nicholls J R. *Materials Science and Technology*[J], 2013, 4: 398
- 33 Khan A, Ullah I, Ullah A et al. *Intermetallics*[J], 2022, 146: 107 571
- 34 Pint B A. *Oxidation of Metals*[J], 1996, 45: 1
- 35 Zhou Y, Peng X, Wang F et al. *Scripta Materialia*[J], 2006, 55: 1039
- 36 Tian L X, Liu W T, Wang K et al. *Materials Chemistry and Physics*[J], 2022, 276: 125 350

309 不锈钢表面 CeO₂ 改性铝化物涂层的循环氧化行为

李钦东, 孟君晟, 陈柏森, 郝晨帆, 陈志辉
(山东交通学院 船舶与港口工程学院, 山东 威海 264200)

摘要: 以 NH₄Cl 为活化剂, 采用包埋法在 309 不锈钢上制备了纳米 CeO₂ 改性铝化物涂层。采用 X 射线衍射分析仪、扫描电子显微镜和能谱仪对涂层以及循环氧化 50 次后的表面和横截面进行了分析。微观结构研究表明, 改性涂层中包含 Fe₂Al₃ 相, 由于基底金属的向外扩散, 改性涂层捕获了少量的 CeO₂ 纳米颗粒。与不添加 CeO₂ 纳米颗粒的普通铝化物涂层相比, 在 900 °C 的大气环境下, 分散 CeO₂ 改性铝化物涂层表现出更好的防氧化剥落性能; 在 50 次循环氧化后, CeO₂ 改性铝化物涂层上仍然可以发现一些 Fe₂Al₃ 相, 并存在向外扩散的 Al 层、中间的 FeAl 层和外部的 Fe₂Al₃+FeAl 混合层, 这表明 CeO₂ 纳米颗粒可以延缓铝化物涂层的降解。

关键词: 包埋法; 铝化物涂层; 活性元素效应; 循环氧化

作者简介: 李钦东, 男, 1998 年生, 硕士生, 山东交通学院船舶与港口工程学院, 山东 威海 264200, 电话: 0631-3998910, E-mail: liqd182@163.com